

Scale-free behavior of weight distributions of connectomes

Michelle Cirunay¹, Géza Ódor¹, István Papp¹ and Gustavo Deco²¹*Institute of Technical Physics and Materials Science, Center for Energy Research, P. O. Box 49, H-1525 Budapest, Hungary*²*Center for Brain and Cognition, Theoretical and Computational Group, Universitat Pompeu Fabra/ICREA, Barcelona, Spain*

(Received 6 August 2024; accepted 8 January 2025; published 5 February 2025)

To determine the precise link between anatomical structure and function, brain studies primarily concentrate on the anatomical wiring of the brain and its topological properties. In this work, we investigate the weighted degree and connection length distributions of the KKI-113 and KKI-18 human connectomes, the fruit fly, and the mouse retina. We find that the node strength (weighted degree) distribution behavior differs depending on the considered scale. On the global scale, the distributions are found to follow a power-law behavior, with a roughly universal exponent close to 3. However, this behavior breaks at the local scale as the node strength distributions of the KKI-18 follow a stretched exponential, and the fly and mouse retina follow the log-normal distribution, respectively, which are indicative of underlying random multiplicative processes and underpins nonlocality of learning in a brain close to the critical state. However, for the case of the KKI-113 and the H01 human (1 mm³) datasets, the local weighted degree distributions follow an exponentially truncated power law, which may hint at the fact that the critical learning mechanism may have manifested at the node level too.

DOI: [10.1103/PhysRevResearch.7.013134](https://doi.org/10.1103/PhysRevResearch.7.013134)

I. INTRODUCTION

In neuroscience, networks-based analysis is heavily needed as the brain is a complex system made up of many interacting neurons [1]. Understanding the structure of these connections is crucial as the form is believed to be highly linked with function [2]. The objective description of the nodes' and edges' contributions to the network as a whole is made possible by the network metrics. Regardless of how widely dispersed or how closely spaced apart they are, nodes with similar qualities can be grouped into a single structurally defined class [3].

In the literature, one may find many attempts to investigate how the morphological and topological quantities are related to neuronal development. For example, earlier works on the structural neural circuits of the cerebral cortex characterized the cortex as a mixing device whose cortico-cortical connections are primarily determined by chance and may be further refined during the learning process [4]. An even older model of neural networks, which Beurle thought might be shaped by learning and plasticity, was based on random connectivity, an unstructured substrate, in parallel with these neuroanatomical concepts [5]. Recently, models were proposed in which network optimization is taken into account. For example, Lynn *et al.* [6] proposed a model in which following a random edge pruning new link is added either by a preferential attachment or randomly. This provides heavy-tailed connection strengths in agreement with the connectomes they considered. Others have even looked at combined topological and spatial

properties of neural networks by making an analogous physical construct of connectomes, which they called *contactomes* [7], and found that optimization with certain boundary conditions leads to degree and distance distributions close to the neural connectomes in the fruit fly, mouse, and human, and unveil a simple set of shared organizing principles across these organisms. While neuronal distance distributions are known to follow exponential rule [8], degree distributions exhibit more fat-tailed-like distribution tails, typically stretched exponential [9]. Scale-free behavior was found at the global level of weights in the case of large human white matter bundles [10] and in the case of neural links of the hemibrain [11].

Brain criticality hypothesis states that the brain activity persists between periods of rapid extinction and amplification [12]. According to theoretical and experimental evidence, the brain functions close to this region [13–17], which optimizes its computational capabilities [12]. In critical dynamics, a common marker of criticality in a system is the presence of power-law distributed quantities. Previously, it has been hypothesized that functional brain networks follow scale-free behaviors characterized by the presence of power laws [18,19]. Power laws signal a certain amount of self-organization, either through replication (as in biological/metabolic networks) or growth and preferential attachment (as in sociological/technological networks) [20,21]. Moreover, it has been proposed that the *scale-free* property enables effective communication using a limited number of core nodes that serve as information flow hubs, such as in the case of transportation networks [22]. Although there are many possible mechanisms that produce power laws [23], critical behavior optimizes information processing. Power laws can therefore be used as a tool to look into the criticality of neural systems data [24].

Published by the American Physical Society under the terms of the Creative Commons Attribution 4.0 International license. Further distribution of this work must maintain attribution to the author(s) and the published article's title, journal citation, and DOI.

TABLE I. Properties of the giant connected components (GCCs) of the considered networks.

Dataset	No. Nodes	No. Edges
KKI-113	799 133	48 096 501
KKI-18	797 759	46 524 003
H01 Human (1 mm ³)	13 579	76 004
Mouse retina	1076	577 350
Fly (hemibrain)	21 662	3 413 160
Fly (hemibrain reciprocated)	16 804	3 251 362
Fly (full brain)	124 778	3 794 527
Fly (full brain filtered)	18 103	157 904
Fly (larva)	2952	110 677

One of the main neural processes that occur during a living organism's lifespan is learning. Learning takes place because of the alterations in the strength and number of connections that happen between existing neurons. Additionally, frequently used pathways are reinforced and decay with inactivity, more formally called long-term potentiation (LTP) and long-term depression (LTD), respectively [25,26]. In this work, we investigate how critical learning mechanisms (function) affect the weight and strength distributions of node connections (form) of human and nonhuman connectomes on both the global and the local scale. In the absence of availability of baby connectome datasets, we utilize a fruit fly larva and adult fruit fly data to study the developmental changes that have occurred.

II. METHODOLOGY

The connectome is defined as the structural network of neural connections in the brain [27]. At the size of a single neuron, existing imaging methods are unable to fully resolve the roughly $\approx 10^{11}$ neurons that make up the human brain. In this work, we employed coarse-grained networks, acquired using diffusion tensor imaging, including $\approx 10^6$ nodes, which is found to agree well with ground-truth data from histology tract tracing [28,29]. Such large, whole-brain network data are obtained from the Open Connectome Project repository and have been previously analyzed [9]. The enormous number of nodes results from the usage of various parcellations that are closer to voxel resolution. For instance, the brain masks of a conventional aligned magnetic resonance imaging (MRI) with 1 mm resolution include about 1.8 million voxels. Here, various connectome datasets are considered: human KKI-113, KKI-18, H01 (1 mm³), fruit fly (various versions with properties detailed below), and the mouse retina. All of these are considered large enough to avoid finite-size limits. Table I shows the network properties of these datasets.

The KKI-113 network contains 799 133 nodes and 48 096 500 weighted and directed edges. On the other hand, the KKI-18 contains 836 733 nodes and 46 524 003 weighted and directed connections [9,30]. Additionally, the human H01 (1 mm³) dataset contains 13 579 nodes and 76 004 edges [7]. To serve as a comparison, we also consider a fly's full brain with 124 778 nodes and 3 794 527 edges and a filtered version, where cells labeled as GLUT, ACH, and GABA were removed following Ref. [31], having 18 103 nodes and 157 904 edges

[32], a fly hemibrain [33] (with 21 662 nodes and 3 413 160 edges) connectomes and its bidirectional version (with 16 804 nodes and 3 251 362 reciprocal edges). Additionally, to investigate the changes in a fly's brain, we included a fly larva dataset [34] with 2952 nodes and 110 677 edges. Finally, we also include the mouse retina data set, with only 1076 nodes and 577 350 weighted and directed edges [35]. The neural mouse retina has the interesting property of exhibiting homeostatic plasticity after the development stages characterized by the remarkable ability to maintain a stable architectural and functional organization [36]. Here, it would be interesting to see how its edge weights and node strength distributions compare with other organisms that exhibit more flexible plasticity over time as a response to external stimuli.

As mentioned in the previous section, we take particular interest in the global and local weight distributions of the datasets that are considered. The global node strength w_i refers to the number of edges that surround a particular node i . In weighted networks, the node strength is the generalization of the node degree or how strongly a node is connected to the rest of the nodes in the networks [37]. The weighted node out-degree (node strength) s_i^{out} is the sum of the edge weights of outgoing edges emanating from node i [37],

$$s_i^{\text{out}} = \sum_j a_{ij} w_{ij}. \quad (1)$$

Here, the weights w_{ij} correspond to the number of links between two nodes in the network and $a_{ij} = 0, 1$ are adjacency matrix elements, describing the connections between nodes i and j . Similarly, the weighted in-degree/strength s_i^{in} is the sum of the incoming edge weights for links incident to that node,

$$s_i^{\text{in}} = \sum_j a_{ji} w_{ji}. \quad (2)$$

Additionally, we also present results on the distribution of the voxel Euclidean distances of the largest human connectome, the KKI-113, in addition to the previously reported topological properties for other human connectomes [9].

III. RESULTS

A. Neuronal distances

To describe the spatial arrangement of KKI-113, we regard nodes whose location coordinates (x, y, z) correspond to its center. Here, we computed the Euclidean distance between them and obtained the distribution displayed in Fig. 1. In the literature, neuronal distances are known to follow the exponential rule $p(d) \propto e^{-d/d_0}$ for the case of the inter-areal cortical network connections in macaques, mice, and rats [8]. Furthermore, there is evidence that the probability of local connections also decays exponentially [38,39]. Previous works have hypothesized that the establishment and maintenance of synapses in neural connectomes is connected to wiring cost, which aligns with the concept of exponential decay [40–42]. By visual inspection, the distribution of the neuronal distances for KKI-113 seems to agree with such a concept with a characteristic value of $d_0 = 15.72$ mm corresponding to the mean of the data. As one may observe,

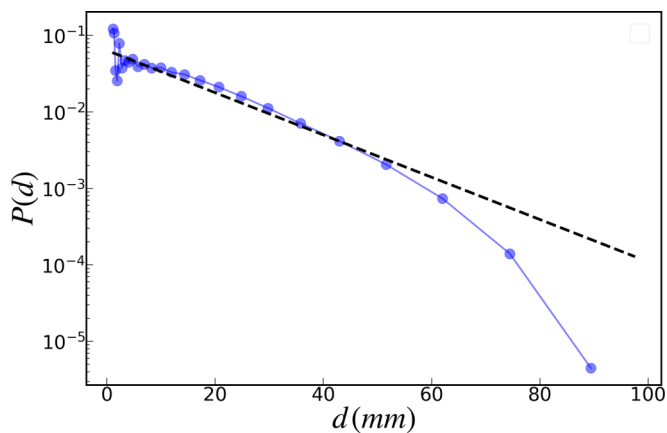


FIG. 1. White matter fiber tract lengths of the KKI-113 are in accordance with the exponential law with a distance scale $d_0 = 15.72$ mm and cross over to an even faster decay for $d > 40$ mm.

the tail is found to decay faster. This may be due to the limitations of the Diffusion Tensor Imaging, which was employed for data acquisition, wherein there is a possibility of underestimating long-distance connections [43,44] and overestimating local connections [45], as in the case of the typical global tractography approach in which streamlines weighted with their corresponding fiber lengths are traced to connect pairs of given voxels [46]. Although a more recent work on the use of diffusion MRI tractography and histological tract tracing applied on ferret brain has shown good agreement between anatomical experiments and the estimates done for the case of mouse and monkey [29], increasing confidence in the technique, we believe that the observed faster decay for the case of KKI-113 was due to this imaging limitation and the fact that the human brain is far more complex and contains more white matter than any other nonhuman primates [47], which may have introduced difficulty in delineating neuronal connections, especially at large distances. Moreover, it has been suggested that in larger brains, long-range connections may require greater axon diameters in order to sustain fast neural transmission [48,49] and that certain types of high-cost connectivity may be less common in larger brains [50].

B. Global weights and local strength distributions

Recent works have shown that the computational complexity of a single biological neuron is equivalent to that of 5–8 layers of deep neural networks (DNNs), which they attributed to the treelike morphology of their dendritic branches [51] as well as to their electrical properties [52,53]. The brain as a complex adaptive system is made up of these individual computational units, whose interactions (i.e., spike-timing-dependent synaptic plasticity (STDP) [54], Hebbian Rules [55], short-term plasticity [56]) can be considered endogenous factors of neural dynamics that drive the brain to criticality [57]. One common indicator of criticality in a system is the presence of power-law distributed quantities and the scaling laws among them. Although there are many other possible mechanisms that produce power laws [23], we note that criticality optimizes information processing [12] and, thus, there is reason to believe that in the context of learning, the presence

TABLE II. Global weight distributions' fitting parameters.

Dataset	Power-law exponent α	KS distance D
KKI-113	3.11(1)	0.040
KKI-18	3.04(1)	0.052
H01 Human (1 mm ³)	3.7(12)	0.057
Mouse retina	3.1(5)	0.087
Fly (hemibrain) (FHB)	3.5(2)	0.013
Fly (hemibrain reciprocated) (FHBR)	3.4(2)	0.019
Fly (full brain) (FFB)	3.06(4)	0.030
Fly (full brain filtered) (FFBF)	3.0(6)	0.17
Fly (larva) (FL)	3.5(3)	0.070

of power law is driven by such mechanism. Power-law distribution analysis can therefore be used to look into the criticality of nervous system data [24]. In the following, we present how the critical learning mechanism influences the global and local weight distributions of the datasets being considered.

Figure 2 shows and Table II summarizes the global weight distributions of the KKI-113, KKI-18, human H01 (1 mm³), mouse retina, the hemi- and full brains of fruit flies, and that of a fruit fly larva. We employed the statistical framework of Clauset *et al.* [58] to identify and measure the power-law behavior. A pure power law allows for arbitrarily large or small values and, because we are dealing with empirical data, we can only fit a power law for a limited range of values. Here, we determine the power law by assuming an x_{\min} (where $x_{\min} > 0$) and via the behavior of the tail of the distribution. We checked the goodness of fit by computing the Kolmogorov-Smirnov (KS) distance D and the standard error coefficient σ (see Sec. 2 of the Appendix for the details of Clauset *et al.*'s KS statistics implementation). The exponent which minimizes the value of the KS distance is displayed in the figure. Here, we find that on the global scale, the distributions are found to follow a power-law behavior, with a roughly universal exponent close to 3. The scale-free behavior allows for effective communication due to the presence of core nodes that serve as information hubs [20,22]. Note that the global weight distribution of the KKI-18 [Fig. 2(b)] has been previously investigated [10], with a power-law fit of $\alpha = 3.05(5)$. This was obtained for data with a size of $N = 41\,523\,931$. This time, however, we obtained a more complete graph with $N = 46\,524\,003$, such that the power-law exponent varied slightly with an exponent of $\alpha = 3.04(1)$.

In the case of the mouse retina [Fig. 2(d)], we observe that its global edge weights also follow a power-law behavior with exponent of ~ 3 , similar to the other organisms. This is despite the fact that unlike the other datasets, the mouse retina is not expected to develop much structural change beyond the development of the mouse (homeostatic plasticity), a necessary adaptive mechanism to ensure the stability of the firing rate in neurons to compensate for prolonged perturbations of neuronal activity, e.g., visual and auditory cortices [59,60].

Figures 2(e) and 2(f) show the edge weight distributions of the fruit fly data sets, where we found that $\alpha_{\text{full}} < \alpha_{\text{larva}}$. The larger exponent value for the larva, indicating a higher

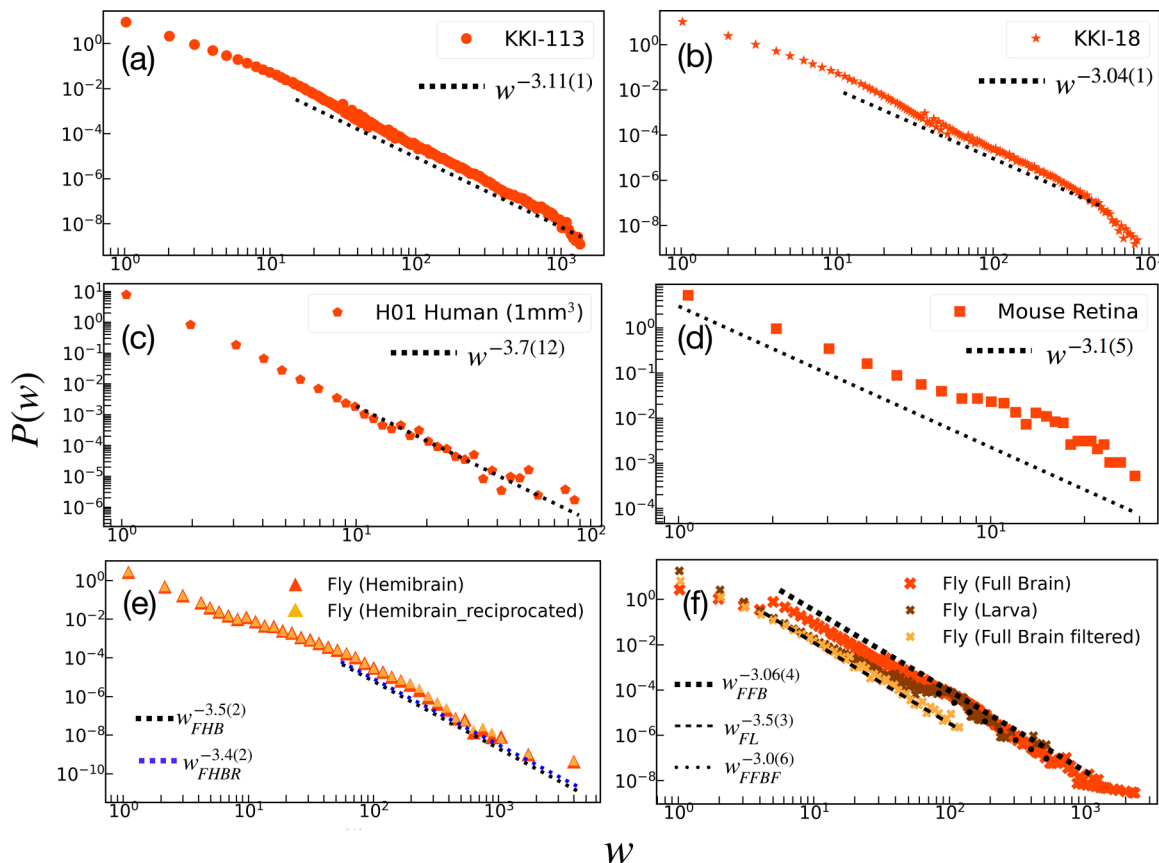


FIG. 2. The weight distributions of (a) KKI-113, (b) KKI-18, (c) H01 human (1 mm³), (d) mouse retina, (e) fly (hemibrain), (f) fly (full brain, and its filtered version), and that of a larva all follow power-law behaviors in the global scale.

probability of finding nodes that have fewer links or weaker connections to its neighbors, can be attributed to the fact that at this stage, the fruit fly is still in its formative stages of development. Moreover, this state of the larva network where there is a lack of large values of edge weights may be thought of as its “prelearning” phase, where neuroplasticity has not yet occurred. Finally, the opposite can be observed for the full brain of an adult fruit fly, which has the lowest value of power-law exponent. This means a lower probability of low-value weights and more likelihood of finding high-edge weights, as indicated by its fat tail. The presence of high-edge weights may be an indication of the structural and functional reinforcements that have occurred throughout the phases of a fly’s development.

We also considered a filtered version of the adult fly’s full brain where the glia cells are removed. Glial cells are non-neuronal cells that create myelin in the peripheral nervous system, helping maintain homeostasis and providing support and protection for neurons [61]. The volumetric ratios of glial cells can vary for every species and every region in their brains [62]. In spite of the inconclusiveness on the ratio of neuron-to-glial cells, we still find value in investigating the case of removing glial cells in the fruit fly, as previous works have shown that these cells in the fruit fly share significant molecular and functional (engulfment activity) attributes with mammalian astrocytes [63,64]. Here, we observe that the exponent of the tails does not vary much with that of the adult

fly’s full brain and the only difference is that there is now a lower probability of finding large edge weights.

If we follow this reasoning, one may ask why the global edge weight distribution of the fly hemibrain, which is taken from an adult fruit fly (both the reciprocated and unidirectional datasets), is steeper than that of a fruit fly larva. One reason is that by itself, the brain of a fly (*Drosophila*) is sparse compared to *C.elegans*, a larva zebra fish, and a mouse [31]. Additionally, this can be due to structural reasons, i.e., the full brain connectome includes peripheral, visual neurons, while the hemibrain only consists of the central nervous system. Finally, the data acquisition when considering only a region may have introduced more complications as, this time, some nodes and their corresponding connections to other regions of the brain may have been cut as well, leading to fewer edges (a preponderance of lower edge weight values) in the considered giant connected cluster (GCC).

Figure 3 shows the local in-, out-, and total (in+out)-node strength distributions for all of the considered datasets. For the case of KKI-113 [Figs. 3(a)–3(c)] and the human H01 (1 mm³) datasets, the strength distributions are found to follow an exponentially truncated power law, also consistent with other large human connectomes [9]. The presence of a power law, albeit truncated, may hint that the critical mechanism is manifested at the node level too [65]. The truncation may be due to some physical constraints. For example, Mossa *et al.* attributed the truncation on the degree distributions of the

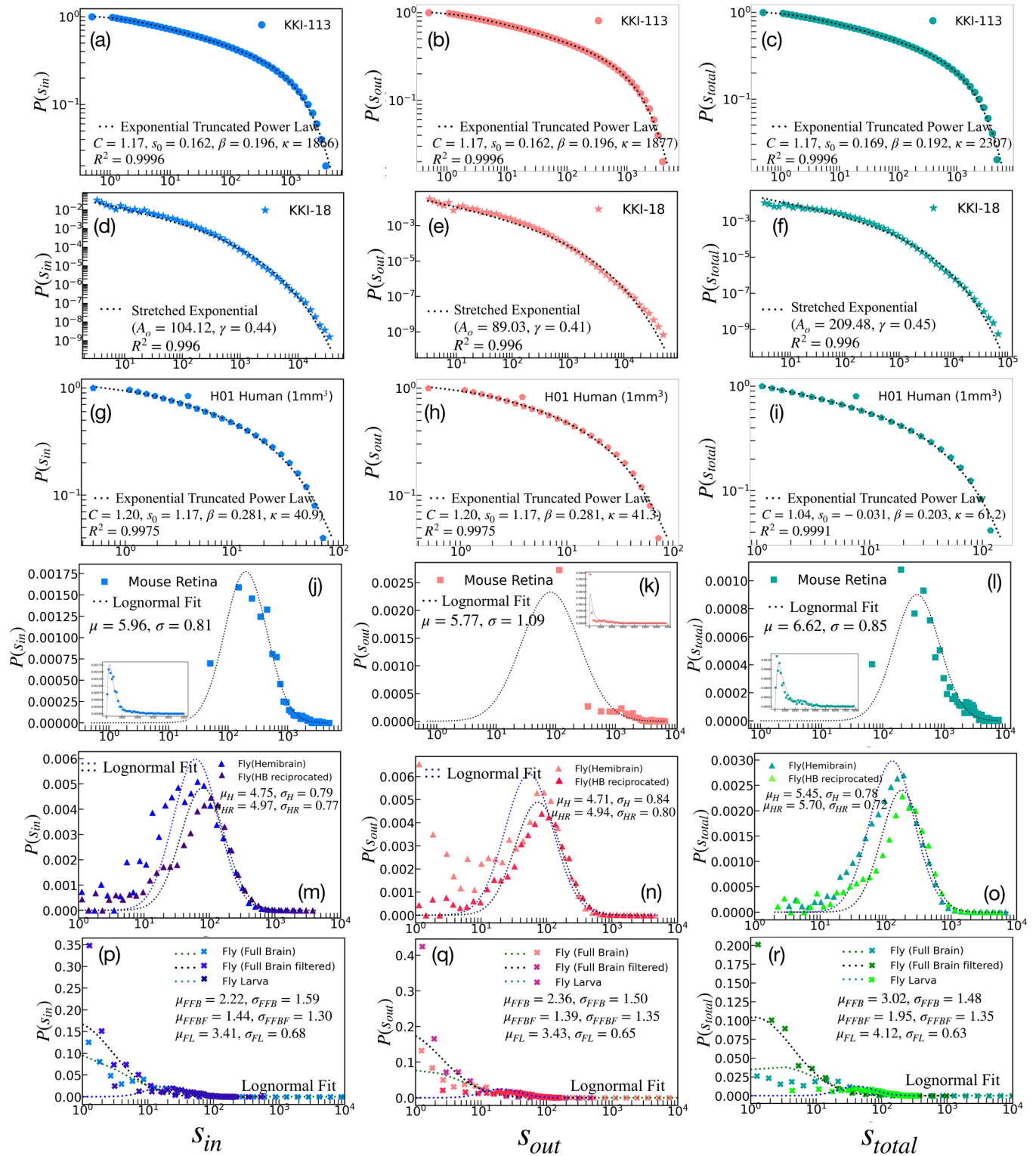


FIG. 3. Local weighted degree (node strength) distributions no longer follow a power-law behavior. (a)–(c) The weighted local in-/out-degrees of the KKI-113 are shown to behave as an exponentially truncated power law. (d)–(f) Meanwhile, KKI-18 follows a stretched exponential. (g)–(i) The human H01 (1 mm³) distributions, on the other hand, follow an exponentially truncated power law. Finally, the weighted degree distributions of the (j)–(l) mouse retina, and the (m)–(o) hemi- and (p)–(r) full brains of a fruit fly and that of a larva, having considerably smaller spatial sizes, all follow log-normal distributions.

TABLE III. Local strength distributions' fitting parameters.

Dataset	Fitting function	Parameters		
		s_{in}	s_{out}	$s_{total} = s_{in} + s_{out}$
KKI-113	Expt. truncated power law	$C = 1.17$	$C = 1.17$	$C = 1.17$
		$s_o = 0.189$	$s_o = 0.189$	$s_o = 0.189$
		$\beta = 0.150$	$\beta = 0.150$	$\beta = 0.147$
		$\kappa = 1371$	$\kappa = 1378$	$\kappa = 1682$
KKI-18	Stretched expt.	$A_o = 104.12$	$A_o = 89.03$	$A_o = 209.48, c = 0.45$
		$\gamma = 0.44$	$\gamma = 0.41$	
H01 Human (1 mm ³)	Expt. truncated power law	$C = 1.20$	$C = 1.20$	$C = 1.20$
		$s_o = 1.17$	$s_o = 1.17$	$s_o = -0.031$
		$\beta = 0.281$	$\beta = 0.281$	$\beta = 0.203$
		$\kappa = 40.9$	$\kappa = 41.3$	$\kappa = 61.2$
Mouse retina	Log-normal	$\mu = 5.96, \sigma = 0.81$	$\mu = 5.77, \sigma = 1.09$	$\mu = 6.62, \sigma = 0.85$
Fly (hemibrain) (FHB)	Log-normal	$\mu = 4.75, \sigma = 0.79$	$\mu = 4.71, \sigma = 0.84$	$\mu = 5.45, \sigma = 0.78$
Fly (hemibrain reciprocated) (FHBR)	Log-normal	$\mu = 4.97, \sigma = 0.77$	$\mu = 4.94, \sigma = 0.80$	$\mu = 5.70, \sigma = 0.72$
Fly (full brain) (FFB)	Log-normal	$\mu = 2.22, \sigma = 1.59$	$\mu = 2.36, \sigma = 1.50$	$\mu = 3.02, \sigma = 1.48$
Fly (full brain filtered) (FFBF)	Log-normal	$\mu = 1.44, \sigma = 1.30$	$\mu = 1.39, \sigma = 1.35$	$\mu = 1.95, \sigma = 1.35$
Fly (larva) (FL)	Log-normal	$\mu = 3.41, \sigma = 0.68$	$\mu = 3.43, \sigma = 0.65$	$\mu = 4.12, \sigma = 0.63$

world wide web (www) and the University of Notre Dame domain to the limitation in information-processing capabilities of the nodes. As there is a cost associated with information processing, there was a need to filter incoming information based on *interest*. By doing so, the new nodes in the network only process a subset of the information from existing nodes [66]. As the brain itself is an information-processing unit, we believe that this may also explain the truncation in the local weighted degree distributions of the KKI-113 and the H01 (1 mm³) datasets, wherein neuronal connections and exchanges only occur with a subset of local neighbors. Additionally, in systems that restrict the maximum number of linkages that a node can have, such as the local neighborhood being considered, the scale-free characteristic is not to be expected. The ability of the nodes to link to an arbitrary number of other nodes is necessary for the scale-free property to appear.

Stretched exponential and log-normal distributions may arise from *multiplicative processes*. In fact, in some cases, Laherre and Sornette proposed the stretched exponential as an alternative to the power law [67]. With multiplicative phenomena, one instance can multiply rapidly, triggering a cascade. When something is of this nature, individual instances are not independent of one another. These behaviors can be expected to arise from a high level of connectivity. Here, we observe that such distributions not only describe the possible types of events or cascade that flow through these connections, i.e., electrical signal, infection, etc., but, this time, they describe the level of connectivity itself (i.e., weighted degree). As shown in Fig. 3 and summarized in Table III, local node strengths (s_{in} , s_{out} , and s_{tot}) of the KKI-18 [Figs. 3(d)–3(f)], the mouse retina [Figs. 3(j)–3(l)], and the fruit fly [Figs. 3(m)–3(r)] are found to follow the stretched exponential or log-normal distributions, respectively. The former is consistent with a previous work on other large human connectomes [9]. We surmise that this multiplicative creation

of connections has resulted from *neuroplasticity* or the brain's ability to functionally and structurally reorganize as a response to external stimuli [68–70]. Such connections are the physical reinforcements that were created during the different stages of development of the human, fruit fly, and mouse.

The formation of synapses in the brain is thought to have begun with a mostly undirected “exploratory” extension, which is followed by selective consolidation and contact dissolution in an early developmental model. The first process might be termed *random*, whereas the second process transmits *specificity* since it is primarily driven by neural activity or biochemical interactions between participating cells [71]. As the brain connections were first thought to be random and later shaped by learning and plasticity [4,5], this may explain the observed log-normal behaviors that hint at the underlying random multiplicative processes that have occurred in the system.

It may appear difficult for spatially embedded networks to exhibit scale-free behavior because of the inherent limitations imposed by basic spatial and metabolic constraints [3] on the density and number of connections that may be maintained at any given node. An exponential and exponentially truncated power law was seen in different spatial networks, including transportation networks [72,73], which we have also observed as in the case of the human connectomes, KKI-113, KKI-18, and H01 (1 mm³), as shown in Figs. 3(a)–3(i). For even more constrained networks such as the case of the mouse retina and fruit fly (hemi, larva, adult), Figs. 3(j)–3(r) show that their node strength (s_{in} , s_{out} , s_{total}) distributions follow the log-normal distribution, characterized by a unimodal heavy-tailed behavior described by the parameters μ and σ (the mean and standard deviation of the natural logarithm of the strengths), representing a characteristic value and variations in node strengths. For these datasets, the proximity in value of the parameters may hint at the degree of symmetry or reciprocity of the connections at the local scale. This so-called reciprocity

TABLE IV. Summary of source and sink nodes.

Dataset	No. source nodes	Max. s_{out}	$\langle s_{out} \rangle$	No. sink nodes	Max. s_{in}	$\langle s_{in} \rangle$
KKI-113	6684	2100	26.55	5686	536	18.03
KKI-18	2270	1663	52.54	2410	1300	53.68
H01 Human (mm ³)	2109	42	4.63	2145	42	4.33
Mouse retina	1	3977	3977	61	913	255.08
Fly (hemibrain)	0			46	250	62.20
Fly (hemibrain reciprocated)	3	17	9.67	1	3	3
Fly (full brain)	8565	640	18.85	8809	766	18.62
Fly (full brain filtered)	2023	31	1.84	2370	39	3.18
Fly (larva)	58	18	7.66	43	38	16.74

of pathways and connectivity has also been observed in the macaque visual cortex [74] and mammalian cortex [75]. This is also shown in the case of the full fly; see [76]. This may be a manifestation of specificity in the form of link consolidation [71]. Expectantly, the values of such parameters for the total (in + out) strength distributions will be slightly larger.

We further witness the concept of specificity in the development of the fruit fly. Comparing the parameters of a larva [34] and that of a full-grown fly [76], we observe that $\mu_{FFB(R)} < \mu_{FL}$ and $\sigma_{FFB(R)} > \sigma_{FL}$. The same trend is observed even if we consider the filtered version of the adult fly brain. The decrease ($\mu_{FFB(R)} < \mu_{FL}$) in the characteristic node strength in the adult fly brain may be due to the dissolution of connections due to some metabolic processes and other constraints [71]. The larger characteristic node strength (degree/connections) in the larva may be because it is still in the random exploratory stages of forming neural connections. Additionally, these connection strengths cannot vary much from each other (smaller σ) as the larva only has very few nodes to connect to, with such connections not yet being reinforced due to external stimuli and factors [68–70]. The opposite is true for the full brain of the adult fruit fly, which contains more nodes and a larger spatial span of connections.

C. Strength distributions of source and sink nodes in the network

Each network node’s contributions to the overall design of a brain network can be measured once it has been defined. The *network participation indices*, which Kötter and Stephan studied, showed areas of relatively densely connected nodes that were receiving (referred to as “receivers”) and emitting (referred to as “senders”) connections [77]. There are instances when these participatory network metrics that they mentioned, such as extremely central nodes, also have high degree. Information transit may be connected to these network participation metrics [3]. In the following, we explore how the distributions of nodes with purely incoming and outgoing edges contribute to the network.

Table IV summarizes the source (nodes with only outgoing edges) and sink (nodes with only incoming edges) nodes with their corresponding average in or out strengths for all the datasets being considered. For KKI-113, (pure) source and sink nodes make up approximately 0.84% and 0.71% of the network, respectively. On the other hand, KKI-18 is made up

of 0.27% source nodes and 0.29% sink nodes. The human H01 (mm³) dataset consists of 15.53% source nodes and 15.80% sink nodes. For the nonhuman connectomes, we find cases of either having little or no source or sink nodes, such as the case of the mouse retina (with only one source node) and a fly hemibrain, both uni- and bidirectional edges dataset, that contain only a few sink nodes. This may be due to the fact that the mouse retina and the fly hemibrain are only sections of an entire organism’s neuronal network. Notice, however, that although these nonhuman connectomes have fewer nodes, they have very high connectivity to the rest of their neighbors, as indicated by their relatively high average node strengths. Meanwhile, for a fly larva, being only in its developmental stages, the source and sink nodes comprise 0.02% and 0.01% of its entire network. Finally, for the full fruit fly brain, we can observe that its source nodes comprise 6.89% of its neuronal network, while its sink nodes make up 7.06% of it. Its filtered version contains 0.11% source nodes and 0.13% sink nodes.

Even though Tables I and IV indicate that these nodes only comprise a small fraction of the networks, some of these nodes serve as hubs, which is evident in the large value of the maximum s_{in} and s_{out} . Because of this, they can be crucial for neural integration and brain communication, making them important participants in cognitive processes. Furthermore, at times of stress, these network regions are prone to disconnecting and malfunctioning [78]. For example, mapping the locations of sources and sinks in a mouse retina revealed that the prefrontal cortex and other higher-order brain regions are the main neuronal output sources for the rest of the brain, while the basal ganglia are important receivers of incoming projections [79]. In this work, we slightly touch on the topic of source and sink in the neuronal networks of humans (KKI-113, KKI-18), the mouse, and a fruit fly. This time, we explore the mouse retina and investigate the strength distributions of the source and sink nodes. Additionally, as in the case of humans, sources are found to be high-influence nodes which inhibit the sink nodes from going into epileptic seizures [80]. Figure 4 shows the probability distributions of the node strengths of the source [$P(s_{out}|s_{in} = 0)$] and sink [$P(s_{in}|s_{out} = 0)$] nodes in the network datasets being considered. Table V summarizes the fitting parameters of this analysis.

Interestingly, for the human connectomes KKI-113, KKI-18, and the human H01 (1 mm³) datasets, the strength distributions of these sources and sinks follow power-law tails

TABLE V. Source and sink node strength parameters.

Datasets	Sinks ($s_{\text{out}} = 0$)		Sources ($s_{\text{in}} = 0$)	
	Fitting	Parameters	Fitting	Parameters
KKI-113	Power law	$\alpha = 2.3(4), D = 0.056$	Power law	$\alpha = 2.1(2), D = 0.056$
KKI-18	Power law	$\alpha = 2.0(3), D = 0.082$	Power law	$\alpha = 2.0(3), D = 0.081$
H01 Human (1 mm ³)	Power law	$\alpha = 4.0(21), D = 0.039$	Power law	$\alpha = 2.5(5), D = 0.075$
Mouse retina	Log-normal	$\mu_1 = 3.09$		
	Mixture	$\sigma_1 = 0.83$		
		$\mu_2 = 5.86$		
		$\sigma_2 = 0.41$		
Fly (hemibrain) (FHB)	Log-normal	$\mu = 3.84$		
		$\sigma = 0.76$		
Fly (hemibrain reciprocated) (FHBR)				
Fly (full brain) (FFB)	Log-normal	$\mu = 2.24$	Log-normal	$\mu = 2.25$
		$\sigma = 1.17$		$\sigma = 1.17$
Fly (full brain filtered) (FFBF)	Log-normal	$\mu = 0.81$	Log-normal	$\mu = 0.28$
		$\sigma = 0.83$		$\sigma = 0.82$
Fly (larva) (FL)	Log-normal	$\mu = 2.68$	Log-normal	$\mu = 1.89$
		$\sigma = 0.52$		$\sigma = 0.53$

which have exponents slightly above 2. Note that for the strength distribution of the H01 source nodes, we find a sharp knee-point (at $s_{\text{in}} \approx 11$) in its distribution followed by a steep tail (with exponent $\alpha \approx 4$). This sharp transition can signal finite-size limitations since we are looking into a 1-mm³-size region. However, for the case of nonhuman connectomes [Figs. 4(e)–4(h)], we observe log-normal behaviors of source and sink node strengths.

The mouse retina is expectantly smaller with only over a thousand nodes and around half a million edges. By examining the distributions of nodes with either only incoming or outgoing edges, we found that there is only one node in the network that has no incoming edges (identified to be node 0 with $s_0^{\text{out}} = 3977$). Such voxel may be part of the retina that is closest to the mouse’s brain, which distributes information to all other neighboring nodes in the network. Additionally, looking at the sink nodes, qualitatively it was observed that after the first peak, there is another rise in the trend before it goes down again. Note that events following log-normal behaviors are independent random variables with mean and standard deviation values that are also independent of each other, which means that it does not matter how we regroup our data. Having said this, we closely inspect the data by splitting it into two: $s_{\text{in}} \leq 97$ and $s_{\text{in}} > 97$. This value was selected because the intermediate bins are empty, signaling a decay of the previous mode and the rise of the second modal curve. Here, we saw that each range of data would follow a log-normal trend and, as a whole, the entire dataset follows a bimodal log-normal distribution (or log-normal mixture). In the literature, such behavior can model the first-order kinetics of chemicals when mixed [81], subsequent waves of a pandemic [82], or market volatility structures [83]. In this context, the log-normal mixture observed in the mouse retina dataset implies clustering and differences in the concentration of connections. Here, we observe that there is a high probability of finding sparsely connected regions and the occurrence of densely connected portions (with more than 100 incoming edges) of sink

nodes. According to earlier research [75], synaptic strengths in the rat visual cortex follow a log-normal distribution with a heavy tail, indicating a higher-than-expected abundance of strong synaptic connections. Furthermore, stronger connections tend to be more heavily clustered [3], which may account for the data point concentration at the log-normal mixture’s second peak.

Finally, for the case of the fruit fly datasets (hemibrain, larva, full brain, and filtered full brain), the in and out strengths of the source and sink nodes still obey the log-normal behavior, which may be hinted at from the behavior of the local weight distributions shown in Figs. 3(j)–3(l). Similar to the in and out node strength distributions, we can still find that $\mu_{FFB} < \mu_{FL}$ and $\sigma_{FFB} > \sigma_{FL}$ [Figs. 3(m)–3(o)]. Notice that this time, $\mu_{FFBF} < \mu_{FL}$ for both the source and sink nodes. This is because there are more nodes in the filtered version of the adult fly’s full brain ($N = 18\,103$) still as compared to the larva’s ($N = 2952$). In any case, we believe that the same underlying mechanisms are responsible for these observations which led to them following the same statistical behaviors.

IV. POSSIBLE EXPLANATION FOR POWER LAWS OF GLOBAL WEIGHT DISTRIBUTIONS

Long-time learning and memory were shown to be induced via the long-term potentiation (LTP) synaptic plasticity, which is related to the longevity (τ) of neighboring neuron pair firing activity [84]. LTP results from coincident activity of pre- and postsynaptic elements, bringing about a facilitation of chemical transmission, that can persist for periods of weeks or months.

According to this, we assume that the weights $w_{ij} \propto \tau$ and their probability density function (PDFs) are also proportional to the correlated activity durations $p(w_{ij}) \propto p(\tau) \propto \tau^{-\alpha}$. Note that a weight decrease in the case of neurons not firing together should also be taken into account to model

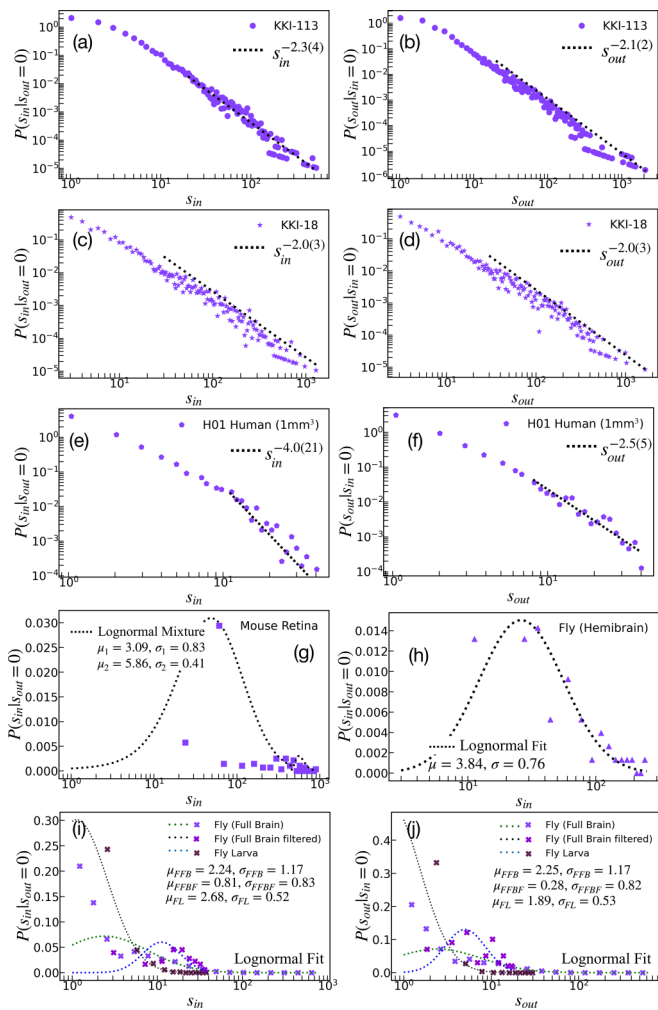


FIG. 4. The weighted in and out strengths of source and sink nodes of (a), (b) KKI-113, (c), (d) KKI-18, (e), (f) H01 human (1mm³), (g) mouse retina (in-strength only), (h) fly (hemibrain) (in-strength only), and (i), (j) fly (larva and full brain).

forgetting and to avoid unbounded growth of w_{ij} , but we assume it to be a random process that does not affect the scaling behavior. The correlated activity duration distributions can be related to the autocorrelation functions of the variables, which exhibit the asymptotic scaling $C_{AA}(t) \propto t^{-\lambda/Z}$, where λ is the autocorrelation exponent and Z is the dynamical exponent of the critical process [85]. Here we consider a pair of active nodes, which in an uncorrelated system exhibits $p_{AA}(t) = p_A(t)^2$, but right at the critical point, $p_{AA}(t) \propto p_A(t)$ [86]. A time integral of the two-point (pair) autocorrelations provides the duration PDFs in the $\tau \rightarrow \infty$ asymptotic limit as

$$\int_{t_0}^{t_0+\tau} C_{AA}(t) dt = p(\tau), \quad (3)$$

where t_0 is the initial time of the avalanche, giving rise to $p(\tau) \sim \tau^{-\alpha} = \tau^{-\lambda/Z+1}$ and an exponent relation $\alpha = \lambda/Z - 1$.

For a generic universality class considered to describe brain criticality [13], i.e., the directed percolation (DP) in the high-dimensional mean-field limit, the autocorrelation function decays asymptotically with $\lambda/Z = 4$ [87], and thus

$p(w_{ij}) \propto p(\tau) \propto \tau^{-3}$ can be expected, in agreement with our measurements for global weight distributions. This scaling can be true for the mean-field behavior of several other basic universality classes, such as DP-C (Manna) or the dynamical percolation [87]. In lower spatial dimensions, the autocorrelation exponent decreases, for example, in $d = 2$, it is $\lambda/Z = 2.5(3)$ [87], providing an estimate $\alpha = 1.5(3)$ for the two-dimensional DP class. Model simulations assuming Manna sandpiles are under way for direct confirmations [88]. We assume that for white matter fiber tracts (i.e., in the case of KKI-18), the aggregate of the neuron level learning rules results in similar distributions.

However, it is still an open question if the critical brain would belong to the mean-field DP universality class or to another class and, if nonuniversal scaling [89,90], corresponding to a Griffiths phase [91] or to an external drive [92,93]. In the case of the Shinomoto-Kuramoto model, possessing periodic external forces, to describe the task phase of the fruit fly brain, it was shown that the PDFs of the interevent times decay with nonuniversal power laws, characterized by exponents $2 < \nu < 4$, depending on the strength of the excitation [93] and on the actual communities. Similar behavior was found for the Hurst and β exponents, which describe autocorrelations. This community dependence has been confirmed via fMRI and blood-oxygen-level-dependent (BOLD) signal measurements [94] in the case of humans.

V. SUMMARY

In summary, we have investigated the weight distributions of various human and animal connectomes to search for power-law-tailed PDFs, which can be related to the learning mechanism of the brain in a critical state. These are the largest, publicly available neural graphs. We found that the global weight distributions can be fitted by power-law tails, characterized by exponents slightly above 3, where the node strength PDFs decay faster, and stretch exponentially or via the log-normal way. The whole brain human fiber tracks, obtained by MRI with deterministic tractography, using the Fiber Assignment by Continuous Tracking algorithm methods [95], exhibit the most power-law-like behavior, and even the node strengths of the source and sink nodes are like that.

We have compared these results of adult (human and animal) connectomes with that of an untrained, larva fly and found that the latter has a narrow PDF, which starts in the same way as the adult fly. This suggests that a certain degree of learning already happens in premature brain development or the initial axon growth mechanisms could also lead to fat tails in the connection strengths [6]. This should be studied more, using other connectomes obtained in the early phase of neural growth.

We provided a possible model and a scaling relation, which connects the critical autocorrelation function to the LTP plasticity mechanism, which can explain the power laws that we observe. Thus we rely on the mutual relationship between structural and functional connectomes and claim that nonlocal learning is dictated by a brain state close to criticality [96]. Assuming mean-field critical behavior of the branching processes, we derive a global weight exponent $\alpha = 3$, which is close to most of the values we obtained by analyzing

different connectomes. But in the lack of the true whole brain function model, we cannot give a precise weight exponent estimate. This can also vary across modules following different dynamics. Note that learning via link strengthening makes the connections more asymmetric, which enhances the violation of the fluctuation dissipation and makes the brains more nonequilibrium [97].

Finally, we have also determined the white matter fiber tract distance distributions of the large KKI-113 human connectome. We found that it follows the exponential rule up to 4 cm size, but breaks down and decays faster for longer lengths. Note that the distances are calculated from the x , y , and z coordinates of nodes as we do not know the real wire lengths.

Overall, the exploration of the relationship between anatomical structure and function across species reveals scale-free properties at the global level and diverse local-scale behaviors of the node structural degree tied to critical dynamics. Our results suggest that human neural architecture achieves a balance between efficiency and adaptability through a dynamic interplay of global and local properties. While highlighting unique patterns in human connectomes, the study situates these within broader principles shared across species, offering insights into the structural basis for learning, self-organization, and adaptability. These findings help us to elucidate the key question about what makes us human.

ACKNOWLEDGMENTS

We are thankful for the helpful discussions with I. A. Kovács, decoding of the KKI-113 coordinates by M. T. Gastner, and the financial support from the Hun-

garian National Research, Development and Innovation Office NKFIH (Grant No. K146736). G.D. was supported by Grant PID2022-136216NB-I00 funded by MICIU/AEI/10.13039/501100011033 and by "ERDF A way of making Europe", ERDF, EU, Project NEurological MEchanismS of Injury, and the project Sleep-like cellular dynamics (Ministerio) (ref. 101071900) funded by the EU ERC Synergy Horizon Europe, AGAUR research support grant (ref. 2021 SGR 00917) funded by the Department of Research and Universities of the Generalitat of Catalunya.

DATA AVAILABILITY

The fitted data are currently available via a request to the authors.

APPENDIX

In this Appendix, we present in detail the methods (i.e., binning, statistical fitting) employed in our analyses.

1. Data binning

a. The logarithmic and linear binning

In this work, we employed both linear and logarithmic binning to our data. We did this because we are dealing with datasets of varying sizes. Figure 5 shows a schematic of the log binning that is employed.

Since the datasets vary in size, the number of bin sets also varies. In general, the number of bin sets ensures that there are no empty bins to avoid erratic trends. The choice of binning, either linear or logarithmic, is based on the number of data

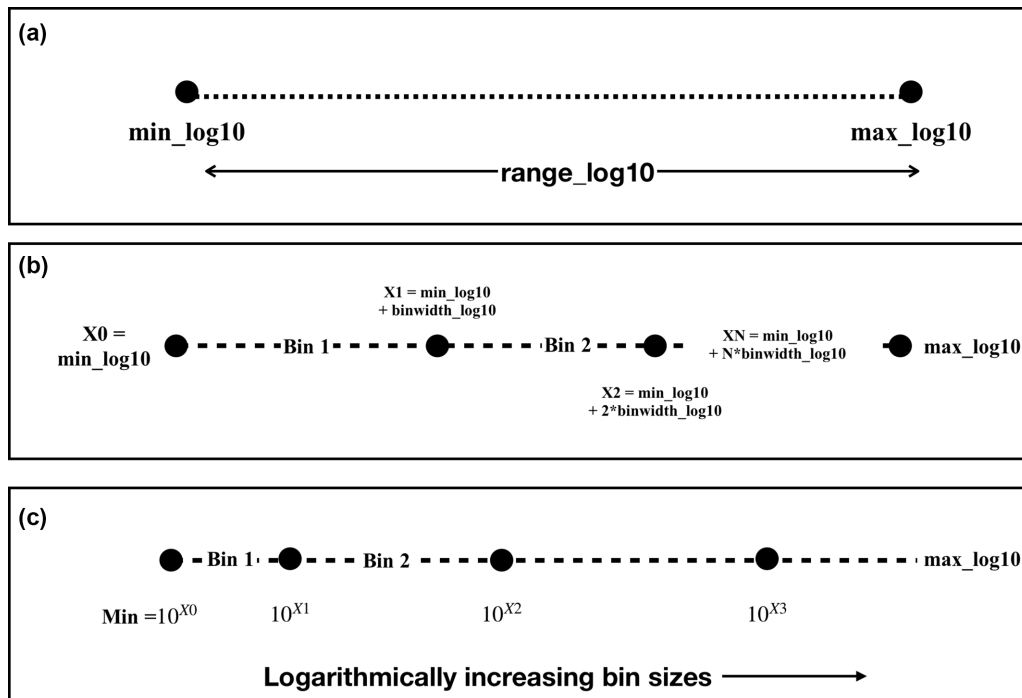


FIG. 5. Schematic of logarithmic binning. (a) To be equally spaced in the logarithmic scale, the range of the data is defined by taking the difference of the logarithm of the minimum and maximum of the data. (b) The range of data is divided by the number of bin sets. The more data points, the larger the number of bins. (c) Logarithmic binning in the linear scale.

TABLE VI. Summary of global weights data and employed binning.

Dataset	No. data points, N	Max. value	Type of binning
KKI-113	48 096 501	1377.0	Logarithmic
KKI-18	46 524 003	854.0	Logarithmic
H01 Human (1 mm ³)	76 004	89	Logarithmic
Mouse retina	577 350	29.0	Linear
Fly (hemibrain)	3 413 160	4299.0	Logarithmic
Fly (hemibrain reciprocated)	3 251 362	4299	Logarithmic
Fly (full brain)	3 794 527	2358.0	Logarithmic
Fly (full brain filtered)	157 904	524.0	Logarithmic
Fly (larva)	110 677	121.0	Linear

points, N , and the maximum value. For the case of linear binning, the same schematics apply, except that we do not take the logarithm of the data points.

In the following, we listed the type of binning employed for every dataset presented in the main text.

b. Global weights distribution

Table VI presents a summary of the global weights data and employed binning.

c. Local node strengths' distribution

Tables VII–X provide a summary of the local node strengths' distribution.

2. The power law

Functional brain networks have been proposed to exhibit scale-free behaviors with power laws present [18,19]. Power laws indicate a specific degree of self-organization, either by growth and preferred attachment or replication, as in biological/metabolic networks [20,21]. When there is a transition from an ordered to an unordered phase without a characteristic length scale, power laws play a crucial role in statistical physics. Both theoretical and practical data support the notion that the brain functions near this important area [13–16].

An observable x follows a power law if it is drawn from the probability distribution

$$P(x) \propto x^{-\alpha}, \quad (\text{A1})$$

where α is a constant parameter of the distribution known as the exponent or scaling parameter. In reality, only a few quantities follow a power law for all values of x . Many times, the power law applies only for values greater than some minimum x_{\min} (where $x_{\min} \geq 0$) such that we say that the tail of the distribution follows a power law. In this work, we fitted our data (Figs. 2 and 4) by employing the methods of Clauset *et al.* [58] implemented by Alstott in PYTHON [98].

Power-law distributions can either be continuous distributions governing continuous real numbers or discrete distributions where the quantity of interest can take only a discrete set of values, typically positive integers.

As we are dealing with the number of edges emanating from a node, we utilize the power law in the discrete case where we only consider integer values with probability distribution of the form

$$P(x) = \Pr(X = x) = Cx^{-\alpha}, \quad (\text{A2})$$

where $x_{\min} > 0$. More details of the normalization constant C and specific form of the parameters α and σ for the discrete power-law distribution case can be found in Ref. [58].

There are many ways to measure the distance between two probability distributions, but for non-normal data, the most common is the Kolmogorov-Smirnov or KS statistic [Eq. (A3)], which is simply the maximum distance between the cumulative distribution function (CDFs) of the data and the fitted model [58]. Note that the KS statistic they used is different from the KS test (which means comparing it with the Kolmogorov distribution). Here, the KS statistic served two purposes: (1) as a distance measure for fitting, wherein they estimate a value \hat{x}_{\min} that minimizes D , and (2) as a distance

TABLE VII. Summary of node in-strength data and employed binning.

Dataset	No. data points, N	Max. value	Type of binning
KKI-113	1 598 266	4977.0	Logarithmic
KKI-18	752 358	38 243.0	Logarithmic
H01 Human (1 mm ³)	13 579	94	Logarithmic
Mouse retina	1076	5000.0	Linear
Fly (hemibrain)	21 662	2708.0	Logarithmic
Fly (hemibrain reciprocated)	16 804	4224.0	Logarithmic
Fly (full brain)	124 778	23 036.0	Logarithmic
Fly (full brain filtered)	18 103	637.0	Logarithmic
Fly (larva)	2952	210.0	Linear

TABLE VIII. Summary of node out-strength data and employed binning.

Dataset	No. data points, N	Max. value	Type of binning
KKI-113	1 598 266	5010.0	Logarithmic
KKI-18	749 667	55 441.0	Logarithmic
H01 Human (1 mm ³)	13 579	95.0	Logarithmic
Mouse retina	1076	6880.0	Linear
Fly (hemibrain)	21 662	5044.0	Logarithmic
Fly (hemibrain reciprocated)	16 804	4378.0	Logarithmic
Fly (full brain)	124 778	12 898.0	Logarithmic
Fly (full brain filtered)	18 103	557.0	Logarithmic
Fly (larva)	2952	160.0	Linear

measure to test the goodness of fit, by using bootstrapping. Instead of using the KS distribution as the distribution for the KS statistic under the null hypothesis, one estimates an empirical distribution for this statistic by simulations. Here, they generated a large number of power-law distributed synthetic datasets with scaling parameter α and lower x_{\min} equal to those of the distribution that best fits the observed data. This distance is compared with distance measurements for comparable synthetic datasets drawn from the same model, and the p value is defined to be the fraction of the synthetic distances that are larger than the empirical distance,

$$D_\alpha = \max_{x \geq x_{\min}} |S(x) - P(x)|, \quad (\text{A3})$$

where $S(x)$ is the CDF of the data for the observations with value at least x_{\min} and $P(x)$ is the CDF for the power-law model that best fits the data in the region $x \geq x_{\min}$. The estimated value of \hat{x}_{\min} is then the value of x_{\min} that minimizes D . Finally, we also computed the standard error σ of our estimate for the power-law exponent.

3. The stretched exponential

To quantitatively account for many reported natural fat-tail distributions in nature and economy, Laherrere and Sornette [67] proposed the stretched exponential (A4) as an alternative to the power law,

$$P(x)dx = c \left(\frac{x^{c-1}}{A_o^c} \right) e^{[\left(\frac{x}{A_o}\right)^c]} dx, \quad (\text{A4})$$

such that the cumulative distribution is

$$P_c(x) = e^{[\left(\frac{x}{A_o}\right)^c]}. \quad (\text{A5})$$

Stretched exponentials are characterized by an exponent $c < 1$, in which the exponent c is the inverse of the number of generations (or products) in a multiplicative process. The borderline $c = 1$ corresponds to the usual exponential distribution. For $c < 1$, the distribution (A5) presents a clear curvature in a log-log plot, while exhibiting a relatively large apparent linear behavior, all the more so, the smaller c is. It can thus be used to account both for a limited scaling regime and a crossover to nonscaling. When using the stretched exponential PDF, the rationale is that the deviations from a power-law description are fundamental and not only a finite-size correction.

Among its numerous benefits is its economy—it has only two movable parameters with definite physical meaning. Moreover, it originates from a straightforward and universal mechanism concerning multiplicative processes.

To find the fitting for the in-, out-, and total-strength distributions, the best-fitting parameters A_o and c (exponent) of the stretched exponential are computed by using the mean and standard deviation of the data and scanning through a range of values for c (from 0.1 to 0.9999).

Adapting from the Appendix of [67], this section shows the derivation of the condition for the data to follow a stretched exponential. We start with the mean of the stretched exponential (A4) given by

$$\langle x \rangle = x_o \left(\frac{1}{c_o} \right) \Gamma \left(\frac{1}{c_o} \right) \quad (\text{A6})$$

TABLE IX. Summary of node total (in + out) node strength data and employed binning.

Dataset	No. data points, N	Max. value	Type of binning
KKI-113	1 598 266	6285.0	Logarithmic
KKI-18	797 759	73 451.0	Logarithmic
H01 Human (1 mm ³)	13 579	159.0	Logarithmic
Mouse retina	1076	7853.0	Linear
Fly (hemibrain)	21 662	7511.0	Logarithmic
Fly (hemibrain reciprocated)	16 804	6394.0	Logarithmic
Fly (full brain)	124 778	26 593.0	Logarithmic
Fly (full brain filtered)	18 103	1194.0	Logarithmic
Fly (larva)	2952	331.0	Linear

TABLE X. Summary of source and sink node strength data and employed binning.

Dataset	Sources $s_{\text{in}} = 0$		Sinks $s_{\text{out}} = 0$		Type of binning
	No. data points, N	Max. value	No. data points, N	Max. value	
KKI-113	6684	2110.0	5686	536	Logarithmic
KKI-18	2270	1663.0	2410	1300	Logarithmic
H01 Human (1 mm ³)	2109	42	2145	42	Logarithmic
Mouse retina	1	3977.0	61	913	Linear (sinks only)
Fly (hemibrain)			46	250	Linear
Fly (hemibrain reciprocated)	3	17.0	1	3	
Fly (full Brain)	8565	640.0	8809	766	Logarithmic
Fly (full brain filtered)	2023	31.0	2370	39.0	Linear
Fly (larva)	58	18.0	43	38	Linear

and its variance is

$$\sigma^2 = x_o^2 \left(\frac{2}{c_o} \right) \Gamma \left(\frac{2}{c_o} \right) - \langle x \rangle^2. \quad (\text{A7})$$

From (A6),

$$x_o = \frac{c_o \langle x \rangle}{\Gamma \left(\frac{1}{c_o} \right)}. \quad (\text{A8})$$

By plugging in (A8) to (A7), we get

$$\sigma^2 = \frac{c_o^2 \langle x \rangle^2}{\Gamma^2 \left(\frac{1}{c_o} \right)} \left(\frac{2}{c_o} \right) \Gamma \left(\frac{2}{c_o} \right) - \langle x \rangle^2. \quad (\text{A9})$$

We simplify (A9) by factoring out $\langle x \rangle$ and get

$$\sigma^2 = \left[2c_o \frac{\Gamma \left(\frac{2}{c_o} \right)}{\Gamma \left(\frac{1}{c_o} \right)} - 1 \right] \langle x \rangle^2. \quad (\text{A10})$$

We transpose $\langle x \rangle^2$ to the other side,

$$\frac{\sigma^2}{\langle x \rangle^2} = \left[2c_o \frac{\Gamma \left(\frac{2}{c_o} \right)}{\Gamma \left(\frac{1}{c_o} \right)} - 1 \right]. \quad (\text{A11})$$

We then add 1 to both sides of (A11),

$$\frac{\sigma^2}{\langle x \rangle^2} + 1 = \left[2c_o \frac{\Gamma \left(\frac{2}{c_o} \right)}{\Gamma \left(\frac{1}{c_o} \right)} \right], \quad (\text{A12})$$

and divide everything by 2 and rearrange,

$$\left[c_o \frac{\Gamma \left(\frac{2}{c_o} \right)}{\Gamma \left(\frac{1}{c_o} \right)} \right] = \frac{\sigma^2}{2\langle x \rangle^2} + \frac{1}{2}. \quad (\text{A13})$$

If we let the left-hand side of (A13) be

$$F_o = \left[c_o \frac{\Gamma \left(\frac{2}{c_o} \right)}{\Gamma \left(\frac{1}{c_o} \right)} \right] \quad (\text{A14})$$

and the right-hand side be some constant F_o which is a function of σ , the standard deviation, and $\langle x \rangle$ is the mean of the data, then

$$F = \frac{\sigma^2}{2\langle x \rangle^2} + \frac{1}{2}. \quad (\text{A15})$$

Here, if the conditions $f = |F - F_o| = 0$ and $c < 1$ are met, then the data follow a stretched exponential trend.

4. The exponential truncated power law

In this work, we used the exponential truncated power law of the form

$$P(x) = C(x + x_o)^{-\beta} \exp(-x/\kappa) \quad (\text{A16})$$

from the work of Gonzalez and Barabási [99]. Simply put, an exponentially truncated power law is a power law multiplied by an exponential function. Since they applied this to displacements r in cities, we replaced the variable r with x to make it into a more general form. Here, the parameter β is the power-law exponent that is valid for small values of s , and κ is the cutoff value. To determine the fitting parameters s_o , β , and κ , we employed the CURVE_FIT() function from PYTHON'S SCIPY.STATS [100]. We used both SCIPY version 1.10.1 with LAPACK 0.3.18 and SCIPY version 1.13.1 with LAPACK 0.3.27. To check the goodness of fit of our data to the said distribution, we compute for the R^2 value, defined as

$$R^2 = 1 - \frac{SS_{\text{res}}}{SS_{\text{tot}}}, \quad (\text{A17})$$

where SS_{res} is the residual sum of squares,

$$SS_{\text{res}} = \sum_i (y_i - f_i)^2, \quad (\text{A18})$$

where y_i is the observed data associated with a fitted or predicted value f_i . On the other hand, the total sum of squares, SS_{tot} , is given by

$$SS_{\text{res}} = \sum_i (y_i - \bar{y})^2, \quad (\text{A19})$$

where \bar{y} is the mean of the data.

5. The log-normal distribution

Based on earlier research [75], synaptic strengths in the rat visual cortex follow a log-normal distribution with a heavy tail, indicating a higher-than-expected abundance of strong synaptic connections. Here, we opted to fit the node strength distributions of the mouse retina with a log-normal distribution as well.

The log-normal distribution is a continuous probability distribution of a random variable whose logarithm is normally distributed. A log-normal process is the statistical realization

of the multiplicative product of many independent random variables, each of which is positive,

$$P(x) = \frac{1}{x\sigma\sqrt{2\pi}} \exp\left(-\frac{(\ln x - \mu)^2}{2\sigma^2}\right), \quad (\text{A20})$$

where μ is the expected value (or mean) and σ is the standard deviation of the variable's natural logarithm, not the expectation and standard deviation of the observed variable

x itself,

$$\mu = \ln\left(\frac{\mu_x^2}{\sqrt{\mu_x^2 + \sigma^2}}\right), \quad (\text{A21})$$

$$\sigma = \ln\left(1 + \frac{\sigma_x^2}{\mu_x^2}\right), \quad (\text{A22})$$

where μ_x and σ_x are the mean and standard deviation of the data.

-
- [1] D. L. Barabási, G. Bianconi, E. Bullmore, M. Burgess, S. Y. Chung, T. Eliassi-Rad, D. George, I. A. Kovács, H. Makse, T. E. Nichols *et al.*, Neuroscience needs network science, *J. Neurosci.* **43**, 5989 (2023).
- [2] W. B. Kristan and P. Katz, Form and function in systems neuroscience, *Curr. Biol.* **16**, R828 (2006).
- [3] O. Sporns, *Networks of the Brain* (MIT Press, Cambridge, 2016).
- [4] V. Braitenberg and A. Schüz, *Cortex: Statistics and Geometry of Neuronal Connectivity* (Springer Science & Business Media, New York, 2013).
- [5] R. L. Beurle, Properties of a mass of cells capable of regenerating pulses, *Philos. Trans. R. Soc. London. Series B: Biolog. Sci.* **240**, 55 (1956).
- [6] C. W. Lynn, C. M. Holmes, and S. E. Palmer, Heavy-tailed neuronal connectivity arises from Hebbian self-organization, *Nat. Phys.* **20**, 484 (2024).
- [7] A. Salova and I. A. Kovács, Combined topological and spatial constraints are required to capture the structure of neural connectomes, *Network Neuroscience* (2024).
- [8] M. Ercsey-Ravasz, N. T. Markov, C. Lamy, D. C. Van Essen, K. Knoblauch, Z. Toroczkai, and H. Kennedy, A predictive network model of cerebral cortical connectivity based on a distance rule, *Neuron* **80**, 184 (2013).
- [9] M. T. Gastner and G. Ódor, The topology of large open connectome networks for the human brain, *Sci. Rep.* **6**, 27249 (2016).
- [10] G. Ódor, Critical dynamics on a large human open connectome network, *Phys. Rev. E* **94**, 062411 (2016).
- [11] G. Ódor, G. Deco, and J. Kelling, Differences in the critical dynamics underlying the human, and fruit-fly connectome, *Phys. Rev. Res.* **4**, 023057 (2022).
- [12] J. M. Beggs and N. Timme, Being critical of criticality in the brain, *Front. Phys.* **3**, 163 (2012).
- [13] J. M. Beggs and D. Plenz, Neuronal avalanches in neocortical circuits, *J. Neurosci.* **23**, 11167 (2003).
- [14] C.-C. Hilgetag, G. A. P. C. Burns, M. A. O'Neill, J. W. Scannell, and M. P. Young, Anatomical connectivity defines the organization of clusters of cortical areas in the macaque and the cat, *Philos. Trans. R. Soc. London B* **355**, 91 (2000).
- [15] W. L. Shew and D. Plenz, The functional benefits of criticality in the cortex, *Neuroscientist* **19**, 88 (2013).
- [16] A. Haimovici, E. Tagliazucchi, P. Balenzuela, and D. R. Chialvo, Brain organization into resting state networks emerges at criticality on a model of the human connectome, *Phys. Rev. Lett.* **110**, 178101 (2013).
- [17] G. Hahn, A. Ponce-Alvarez, C. Monier, G. Benvenuti, A. Kumar, F. Chavane, G. Deco, and Y. Frégnac, Spontaneous cortical activity is transiently poised close to criticality, *PLoS Comput. Biol.* **13**, e1005543 (2017).
- [18] V. M. Eguiluz, D. R. Chialvo, G. A. Cecchi, M. Baliki, and A. V. Apkarian, Scale-free brain functional networks, *Phys. Rev. Lett.* **94**, 018102 (2005).
- [19] M. P. van den Heuvel, C. J. Stam, M. Boersma, and H. E. H. Pol, Small-world, and scale-free organization of voxel-based resting-state functional connectivity in the human brain, *Neuroimage* **43**, 528 (2008).
- [20] A.-L. Barabási and R. Albert, Emergence of scaling in random networks, *Science* **286**, 509 (1999).
- [21] F. Piekniewski, Robustness of power laws in degree distributions for spiking neural networks, in *2009 International Joint Conference on Neural Networks, Atlanta, GA* (IEEE, Piscataway, NJ, 2009), pp. 2541–2546.
- [22] R. Zucca, X. D. Arsiwalla, H. Le, M. Rubinov, A. Gurguí, and P. Verschure, The degree distribution of human brain functional connectivity is generalized pareto: A multiscale analysis, *BioRxiv*, doi:10.1101/840066.
- [23] J. Touboul and A. Destexhe, Power-law statistics and universal scaling in the absence of criticality, *Phys. Rev. E* **95**, 012413 (2017).
- [24] J. Tinker and J. L. P. Velazquez, Power law scaling in synchronization of brain signals depends on cognitive load, *Front. Syst. Neurosci.* **8**, 73 (2014).
- [25] M. T. Owens and K. D. Tanner, Teaching as brain changing: Exploring connections between neuroscience and innovative teaching, *CBE—Life Sci. Edu.* **16**, fe2 (2017).
- [26] J. M. Park, S.-C. Jung, and S.-Y. Eun, Long-term synaptic plasticity: Circuit perturbation and stabilization, *Korean J. Physiol. Pharmacol.* **18**, 457 (2014).
- [27] O. Sporns, G. Tononi, and R. Kötter, The human connectome: A structural description of the human brain, *PLoS Comput. Biol.* **1**, e42 (2005).
- [28] B. A. Landman, A. J. Huang, A. Gifford, D. S. Vikram, I. A. L. Lim, J. A. D. Farrell, J. A. Bogovic, J. Hua, M. Chen, S. Jarso *et al.*, Multi-parametric neuroimaging reproducibility: A 3-t resource study, *Neuroimage* **54**, 2854 (2011).
- [29] C. Delettre, A. Messé, L.-A. Dell, O. Foubet, K. Heuer, B. Larrat, S. Meriaux, J.-F. Mangin, I. Reillo, C. de Juan Romero *et al.*, Comparison between diffusion MRI tractography and histological tract-tracing of cortico-cortical structural connectivity in the ferret brain, *Network Neurosci.* **3**, 1038 (2019).
- [30] Open connectome project, <https://neurodata.io>.
- [31] A. Lin, R. Yang, S. Dorkenwald, A. Matsliah, A. R. Sterling, P. Schlegel, S.-C. Yu, C. E. McKellar, M. Costa, K. Eichler *et al.*, Network statistics of the whole-brain connectome of drosophila, *Nature (London)* **634**, 153 (2024).

- [32] Flywire connectome data, <https://codex.flywire.ai/api/download>.
- [33] The Hemibrain dataset (v 1.0.1), <https://github.com/FlyBrainLab/datasets/blob/main/hemibrain/v1.0.1/README.md>.
- [34] M. Winding, B. D. Pedigo, C. L. Barnes, H. G. Patsolic, Y. Park, T. Kazimiars, A. Fushiki, I. V. Andrade, A. Khandelwal, Javier Valdes-Aleman, F. Li, N. Randel, E. Barsotti, A. Correia, R. D. Fetter, V. Hartenstein, C. E. Priebe, J. T. Vogelstein, A. Cardona, and M. Zlatic, The connectome of an insect brain, *Science* **379**, eadd9330 (2023).
- [35] <https://neurodata.io/project/connectomes>.
- [36] E. Strettoi, B. Di Marco, N. Orsini, and D. Napoli, Retinal plasticity, *Intl. J. Mol. Sci.* **23**, 1138 (2022).
- [37] A. Barrat, M. Barthelemy, Romualdo Pastor-Satorras, and A. Vespignani, The architecture of complex weighted networks, *Proc. Natl. Acad. Sci. USA* **101**, 3747 (2004).
- [38] N. T. Markov, Maria M Ercsey-Ravasz, A. R. R. Gomes, C. Lamy, L. Magrou, J. Vezoli, P. Misery, A. Falchier, R. Quilodran, M.-A. Gariel *et al.*, A weighted and directed interareal connectivity matrix for macaque cerebral cortex, *Cereb. Cortex* **24**, 17 (2014).
- [39] A. C. Kurth, J. Albers, M. Diesmann, and S. J. van Albada, Cell-type specific projection patterns promote balanced activity in cortical microcircuits, *bioRxiv*, doi:10.1101/2024.10.03.616539.
- [40] Y.-Y. Ahn, H. Jeong, and B. J. Kim, Wiring cost in the organization of a biological neuronal network, *Physica A: Stat. Mech. Appl.* **367**, 531 (2006).
- [41] E. Bullmore and O. Sporns, The economy of brain network organization, *Nat. Rev. Neurosci.* **13**, 336 (2012).
- [42] B. L. Chen, D. H. Hall, and D. B. Chklovskii, Wiring optimization can relate neuronal structure and function, *Proc. Natl. Acad. Sci. USA* **103**, 4723 (2006).
- [43] L. Li, J. K. Rilling, T. M. Preuss, M. F. Glasser, F. W. Damen, and X. Hu, Quantitative assessment of a framework for creating anatomical brain networks via global tractography, *NeuroImage* **61**, 1017 (2012).
- [44] V. J. Wedeen, R. P. Wang, J. D. Schmahmann, T. Benner, W.-Y. I. Tseng, G. Dai, D. N. Pandya, P. Hagmann, H. D'Arceuil, and A. J. de Crespigny, Diffusion spectrum magnetic resonance imaging (DSI) tractography of crossing fibers, *Neuroimage* **41**, 1267 (2008).
- [45] S. Jbabdi and H. Johansen-Berg, Tractography: Where do we go from here? *Brain Connectivity* **1**, 169 (2011).
- [46] H. Finger, M. Bönstrup, B. Cheng, A. Messé, C. Hilgetag, G. Thomalla, C. Gerloff, and P. König, Modeling of large-scale functional brain networks based on structural connectivity from DTI: Comparison with EEG derived phase coupling networks and evaluation of alternative methods along the modeling path, *PLoS Comput. Biol.* **12**, e1005025 (2016).
- [47] P. T. Schoenemann, M. J. Sheehan, and L. D. Glotzer, Prefrontal white matter volume is disproportionately larger in humans than in other primates, *Nat. Neurosci.* **8**, 242 (2005).
- [48] J. Karbowski, Global, and regional brain metabolic scaling, and its functional consequences, *BMC Biol.* **5**, 18 (2007).
- [49] J. L. Ringo, R. W. Doty, S. Demeter, and P. Y. Simard, Time is of the essence: A conjecture that hemispheric specialization arises from interhemispheric conduction delay, *Cereb. Cortex* **4**, 331 (1994).
- [50] K. A. Phillips, C. D. Stimpson, J. B. Smaers, M. A. Raghanti, B. Jacobs, A. Popratiloff, P. R. Hof, and C. C. Sherwood, The corpus callosum in primates: Processing speed of axons and the evolution of hemispheric asymmetry, *Proc. R. Soc. B.* **282**, 20151535 (2015).
- [51] D. Beniaguev, I. Segev, and M. London, Single cortical neurons as deep artificial neural networks, *Neuron* **109**, 2727 (2021).
- [52] J. P. Miller, Computer modelling at the single-neuron level, *Nature (London)* **347**, 783 (1990).
- [53] N. Brunel, V. Hakim, and Magnus J. E. Richardson, Single neuron dynamics and computation, *Curr. Opin. Neur.* **25**, 149 (2014).
- [54] F. Effenberger, J. Jost, and A. Levina, Self-organization in balanced state networks by STDP and homeostatic plasticity, *PLoS Comput. Biol.* **11**, e1004420 (2015).
- [55] L. de Arcangelis and H. J. Herrmann, Learning as a phenomenon occurring in a critical state, *Proc. Natl. Acad. Sci. USA* **107**, 3977 (2010).
- [56] A. Levina, J. M. Herrmann, and T. Geisel, Dynamical synapses causing self-organized criticality in neural networks, *Nat. Phys.* **3**, 857 (2007).
- [57] Y. Tian, Z. Tan, H. Hou, G. Li, A. Cheng, Y. Qiu, K. Weng, C. Chen, and P. Sun, Theoretical foundations of studying criticality in the brain, *Network Neurosci.* **6**, 1148 (2022).
- [58] A. Clauset, C. R. Shalizi, and Mark E. J. Newman, Power-law distributions in empirical data, *SIAM Rev.* **51**, 661 (2009).
- [59] M. Teichert, L. Liebmann, C. A. Hübner, and J. Bolz, Homeostatic plasticity and synaptic scaling in the adult mouse auditory cortex, *Sci. Rep.* **7**, 17423 (2017).
- [60] G. G. Turrigiano, The self-tuning neuron: Synaptic scaling of excitatory synapses, *Cell* **135**, 422 (2008).
- [61] K. R. Jessen and R. Mirsky, Glial cells in the enteric nervous system contain glial fibrillary acidic protein, *Nature (London)* **286**, 736 (1980).
- [62] A. Verkhratsky, M. S. Ho, R. Zorec, and V. Parpura, The concept of neuroglia, *Neuroglia in Neurodegenerative Diseases*, Advances in Experimental Medicine and Biology (Springer, Singapore, 2019), pp. 1–13.
- [63] M. A. Logan and M. R. Freeman, The scoop on the fly brain: Glial engulfment functions in drosophila, *Neuron Glia Biol.* **3**, 63 (2007).
- [64] M. R. Freeman, Drosophila central nervous system glia, *Cold Spring Harb. Perspect. Biol.* **7**, a020552 (2015).
- [65] H. S. Ansell and I. A. Kovács, Unveiling universal aspects of the cellular anatomy of the brain, *Commun. Phys.* **7**, 184 (2024).
- [66] S. Mossa, M. Barthelemy, H. E. Stanley, and L. A. Nunes Amaral, Truncation of power law behavior in “scale-free” network models due to information filtering, *Phys. Rev. Lett.* **88**, 138701 (2002).
- [67] J. Laherrere and D. Sornette, Stretched exponential distributions in nature and economy: “Fat tails” with characteristic scales, *Eur. Phys. J. B* **2**, 525 (1998).
- [68] J. Grafman, Conceptualizing functional neuroplasticity, *J. Commun. Disorders* **33**, 345 (2000).
- [69] R. J. Davidson and B. S. McEwen, Social influences on neuroplasticity: Stress and interventions to promote well-being, *Nat. Neurosci.* **15**, 689 (2012).

- [70] B. S. McEwen, Redefining neuroendocrinology: Epigenetics of brain-body communication over the life course, *Front. Neuroendocrinol.* **49**, 8 (2018).
- [71] J. D. Jontes and S. J. Smith, Filopodia, spines, and the generation of synaptic diversity, *Neuron* **27**, 11 (2000).
- [72] L. A. Nunes Amaral, A. Scala, M. Barthelemy, and H. E. Stanley, Classes of small-world networks, *Proc. Natl. Acad. Sci. USA* **97**, 11149 (2000).
- [73] R. Guimera, S. Mossa, A. Turtschi, and L. A. N. Amaral, The worldwide air transportation network: Anomalous centrality, community structure, and cities' global roles, *Proc. Natl. Acad. Sci. USA* **102**, 7794 (2005).
- [74] D. J. Felleman and D. C. Van Essen, Distributed hierarchical processing in the primate cerebral cortex, *Cereb. Cortex* **1**, 1 (1991).
- [75] S. Song, P. J. Sjöström, M. Reigl, S. Nelson, and D. B. Chklovskii, Highly nonrandom features of synaptic connectivity in local cortical circuits, *PLoS Biol.* **3**, e68 (2005).
- [76] S. Dorkenwald, A. Matsliah, A. R. Sterling, P. Schlegel, S.-c. Yu, C. E. McKellar, A. Lin, M. Costa, K. Eichler, Y. Yin, W. Silversmith, Casey Schneider-Mizell, C. S. Jordan, D. Brittain, A. Halageri, K. Kuehner, O. Ogedengbe, R. Morey, J. Gager, K. Kruk, E. Perlman, R. Yang, D. Deutsch, D. Bland, M. Sorek, R. Lu, T. Macrina, K. Lee, J. A. Bae, S. Mu, B. Nehoran, E. Mitchell, S. Popovych, J. Wu, Z. Jia, M. A. Castro, N. Kemnitz, D. Ih, A. S. Bates, N. Eckstein, J. Funke, F. Collman, D. D. Bock, G. S. X. E. Jefferis, H. S. Seung, M. Murthy, and The FlyWire Consortium, Neuronal wiring diagram of an adult brain, *Nature* **634**, 124 (2024).
- [77] R. Kötter and K. E. Stephan, Network participation indices: Characterizing component roles for information processing in neural networks, *Neural Networks* **16**, 1261 (2003).
- [78] M. P. Van den Heuvel and O. Sporns, Network hubs in the human brain, *Trends Cognitive Sci.* **17**, 683 (2013).
- [79] L. Coletta, M. Pagani, J. D. Whitesell, J. A. Harris, B. Bernhardt, and A. Gozzi, Network structure of the mouse brain connectome with voxel resolution, *Sci. Adv.* **6**, eabb7187 (2020).
- [80] K. M. Gunnarsdottir, A. Li, R. J. Smith, J.-Y. Kang, A. Korzeniewska, N. E. Crone, A. G. Rouse, J. J. Cheng, M. J. Kinsman, P. Landazuri *et al.*, Source-sink connectivity: A novel interictal EEG marker for seizure localization, *Brain* **145**, 3901 (2022).
- [81] A. Andersson, Mechanisms for log normal concentration distributions in the environment, *Sci. Rep.* **11**, 16418 (2021).
- [82] P. S. Valvo, A bimodal log-normal distribution model for the prediction of Covid-19 deaths, *Appl. Sci.* **10**, 8500 (2020).
- [83] D. Brigo and F. Mercurio, Log-normal-mixture dynamics and calibration to market volatility smiles, *Intl. J. Theor. Appl. Finan.* **05**, 427 (2002).
- [84] S. F. Cooke and T. V. P. Bliss, Plasticity in the human central nervous system, *Brain* **129**, 1659 (2006).
- [85] G. Ódor, *Universality in Nonequilibrium Lattice Systems: Theoretical Foundations* (World Scientific, Singapore, 2008).
- [86] R. D. Schram and G. T. Barkema, Critical exponents of the pair contact process with diffusion, *J. Stat. Mech.* (2012) P03009.
- [87] M. Henkel, H. Hinrichsen, and S. Lübeck, *Nonequilibrium Phase Transitions*, Vol. 1 (Springer Science & Business Media, New York, 2008).
- [88] M. T. Cirunay, G. Odor, and R. C. Batac, Dynamical evolution of a sandpile-based model on a hierarchical modular network (unpublished).
- [89] M. A. Muñoz, Colloquium: Criticality and dynamical scaling in living systems, *Rev. Mod. Phys.* **90**, 031001 (2018).
- [90] G. Ódor, M. T. Gastner, J. Kelling, and G. Deco, Modelling on the very large-scale connectome, *J. Phys.: Complexity* **2**, 045002 (2021).
- [91] R. B. Griffiths, Nonanalytic behavior above the critical point in a random Ising ferromagnet, *Phys. Rev. Lett.* **23**, 17 (1969).
- [92] D. J. Korchinski, J. G. Orlandi, S.-W. Son, and J. Davidsen, Criticality in spreading processes without timescale separation and the critical brain hypothesis, *Phys. Rev. X* **11**, 021059 (2021).
- [93] G. Ódor, I. Papp, S. Deng, and J. Kelling, Synchronization transitions on connectome graphs with external force, *Front. Phys.* **11**, 1150246 (2023).
- [94] J. K. Ochab, M. Watorek, A. Ceglarek, M. Fafrowicz, K. Lewandowska, T. Marek, B. Sikora-Wachowicz, and P. Oswiecimka, Task-dependent fractal patterns of information processing in working memory, *Sci. Rep.* **12**, 17866 (2022).
- [95] S. Mori, B. J. Crain, V. P. Chacko, and Peter C. M. V. Zijl, Three-dimensional tracking of axonal projections in the brain by magnetic resonance imaging, *Annals Neurol.: Official J. Amer. Neurol. Assoc. Child Neurol. Soc.* **45**, 265 (1999).
- [96] M. Angiolelli, S. Scarpetta, P. Sorrentino, E. T. Lopez, M. Quarantelli, C. Granata, G. Sorrentino, V. Palmieri, G. Messuti, M. Stefano, S. Filippi, C. Cherubini, A. Loppini, and L. Chiodo, Criticality explains structure-function relationships in the human brain, *bioRxiv*, doi:10.1101/2024.07.15.603226.
- [97] J. M. Monti, Y. S. Perl, E. Tagliazucchi, M. Kringelbach, and G. Deco, The fluctuation-dissipation theorem and the discovery of distinctive off-equilibrium signatures of brain states, *bioRxiv*, doi:10.1101/2024.04.04.588056.
- [98] J. Alstott, E. Bullmore, and D. Plenz, POWERLAW: A PYTHON package for analysis of heavy-tailed distributions, *PLoS One* **9**, e85777 (2014).
- [99] M. C. Gonzalez, C. A. Hidalgo, and A.-L. Barabasi, Understanding individual human mobility patterns, *Nature (London)* **453**, 779 (2008).
- [100] P. Virtanen, R. Gommers, T. E. Oliphant, M. Haberland, T. Reddy, D. Cournapeau, E. Burovski, P. Peterson, W. Weckesser, J. Bright *et al.*, SCIPY 1.0: Fundamental algorithms for scientific computing in PYTHON, *Nat. Methods* **17**, 261 (2020).